Classification of wave modes extracted from passive data at Moere Vest

Jason P. Chang and Biondo Biondi

ABSTRACT

By performing multi-component seismic interferometry on passive seismic data from the Moere Vest ocean-bottom node survey, we observe three distinct wave modes from the resulting virtual source gathers: Scholte waves, guided acoustic waves, and critical refractions. Scholte waves are characterized by their dispersive nature, very low frequency content (below 0.5 Hz), slow propagation velocity ($500 - 700$ m/s), and relative clarity in the vertical-vertical correlations. Guided acoustic waves trapped between the sea surface and sea bottom are characterized by their dispersive nature, group velocity of approximately 1500 m/s, and relative clarity in the hydrophone-hydrophone correlations. Critical refractions in the vertical-vertical correlations are characterized by their non-dispersive linear moveout and high propagation velocity ($4000 - 5000$ m/s). Comparison of these events to critical refractions off the top of basalt in vertical-component receiver gathers from active data reveals similar arrival times and moveout velocities. To enhance the clarity of these refractions, we create virtual super-source gathers for both vertical-vertical and vertical-radial correlations. We find that the critical refraction arrives later in the vertical-radial gathers than in the vertical-vertical gathers, which is also observed in vertical- and radial-component receiver gathers from active data. Forward wavefield propagation suggests that these critical refractions could be generated by low-frequency Scholte waves scattering off the horst-and-graben structure of the top of basalt. Overall, these results lay the foundation for passive subsurface imaging using wave modes beyond interface waves.

INTRODUCTION

The application of seismic interferometry to recordings of Earth's ambient seismic noise field has been shown to successfully estimate the Green's function between pairs of receivers. While extraction of the interface-wave portion of the estimated Green's function has been successful across many spatial scales in both land and marine environments (e.g., Shapiro et al., 2005; Bensen et al., 2008; de Ridder and Dellinger, 2011; Chang et al., 2016), there have been far fewer studies that have successfully extracted non-interface-wave portions. In land environments, Roux et al. (2005) and Gerstoft et al. (2008) retrieved diving P-waves at the regional scale. Additionally, Poli et al. (2012) retrieved P-wave reflections off the mantle transition zone, while Ruigrok

et al. (2011) and Zhan et al. (2010) retrieved P- and S-wave reflections off the Moho, respectively. At the exploration scale, Nakata et al. (2015) were able to extract diving P-waves from a dense array at Long Beach, California, while Nakata et al. (2011) and Draganov et al. (2013) were able to extract reflection events in separate locations. In shallow marine environments, studies have been able to extract direct P-waves traveling in the water column (e.g., Mordret et al., 2013; Chang, 2017), as well as sea-surface reflected and sea-bottom reflected events (e.g., Brooks and Gerstoft, 2009).

In this report, we focus on extracting both interface waves and non-interface waves from passive seismic data recorded by the Moere Vest deep-water ocean-bottom node (OBN) array. The work shown here builds on the initial analysis of the continuous recordings performed by de Ridder (2014). We begin with an overview of the Moere Vest OBN array. We then provide an overview of passive seismic interferometry (or ambient-noise cross-correlation technique) and apply it to passive seismic data below 2 Hz. The resulting virtual source gathers reveal three distinct wave modes:

- Scholte waves, which are commonly observed in ambient noise studies using OBN data;

- guided acoustic waves, which have previously only been observed at these water depths and frequencies in Hatchell and Mehta (2010); and

- critical refractions, which have previously never been observed in passive seismic data at this spatial scale.

Because of the rarity of two of these wave modes in passive seismic studies, we outline evidence supporting each of these classifications. We then simulate wave propagation through a simple elastic model to test a hypothesis for the generation of critical refractions from passive energy.

MOERE VEST CONTINUOUS RECORDINGS

The Moere Vest data set, provided by Seabed Geosolutions, consists of 179 four-component ocean-bottom nodes (OBNs) deployed in a line along the seabed in the North Sea and above a block of basalt (Figure 1). The array is notable for its spatial extent (85 km maximum offset between nodes) and deep-water environment (approximately $1.6 - 1.9$ km depth). The nodes consist of three different geometries: 141 nodes spaced 250 m apart and spanning 35 km that form the regular spread; 12 nodes spaced 5 km apart at each end of the regular spread to increase the total length of the array to 85 km; and 26 nodes spaced 2 m apart in two parallel lines along the regular spread. Each node records continuously at 2-ms sampling for approximately 10 days, with all nodes simultaneously recording for 7 of those days.

Within the 7 days of simultaneous recordings were periods of active seismic shooting. This is apparent in the log-spectrogram of the vertical-geophone recording for the

Figure 1: Map of the Moere Vest OBN array. Red points indicate nodes used for spectrograms and virtual source locations. [**CR**]
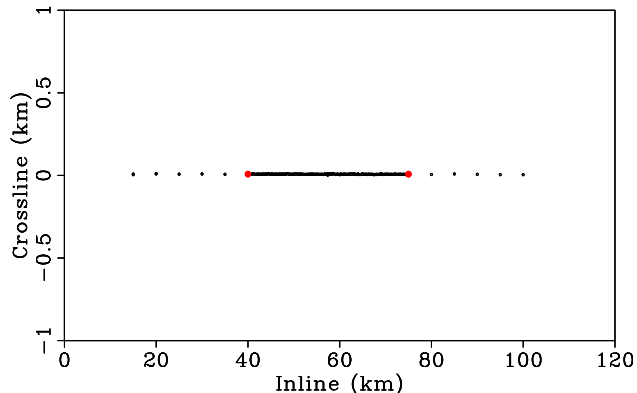
node on the western edge of the regular spread, where the spectral comb signature of active sources is dominant above 2 Hz (Figure 2a). While the effect of active seismic shooting does not appear to interfere with the frequencies of interest in this study (below 2 Hz), we remove them from further analysis to ensure that the results shown here are derived from strictly passive seismic data. Removal of times of active seismic surveys results in about 3 days of simultaneous passive recordings. The resulting log-spectrogram indicates strong microseism energy below 2 Hz (Figure 2b). We look to extract coherent wave modes from this energy using passive seismic interferometry.

PASSIVE SEISMIC INTERFEROMETRY

Passive seismic interferometry produces an estimate of the Green's function between two receivers by cross-correlating their continuous and simultaneous recordings of ambient seismic noise (Wapenaar et al., 2010). Here, we apply processing steps similar to those outlined in Bensen et al. (2007) to the hydrophone and geophone components. First, we rotate the horizontal components of each geophone such that one component is inline with the array and the other component is orthogonal to the array using the method from Alves (2017). We then divide each continuous recording into two-hour windows with 50% overlap (Seats et al., 2012) and remove the time windows containing active seismic shooting (resulting in 78 time windows spanning over 3 days). Next, we perform passive seismic interferometry by calculating the average of the whitened coherency between each pair of nodes across all time windows. This procedure is also referred to as calculating the cross-coherence, and it typically produces a broader-band signal than standard cross-correlation while maintaining phase information. In the frequency domain, the procedure is generally expressed as:

$$[G(x_B, x_A, \omega) + G^*(x_B, x_A, \omega)] = \left\langle \left(\frac{U(x_B, \omega)}{\{|U(x_B, \omega)|\}} \right) \left(\frac{U^*(x_A, \omega)}{\{|U(x_A, \omega)|\}} \right) \right\rangle, \quad (1)$$

where G is the Green's function between two receiver locations (x_A, x_B), $U(x, \omega)$ is the Fourier transform of the wavefield at a given receiver location x, $*$ is the complex conjugate, $\langle \cdot \rangle$ is an averaging operation, $|\cdot|$ is the magnitude of the spectrum, and $\{\cdot\}$ is a 0.003 Hz running window average used for normalizing the signal.
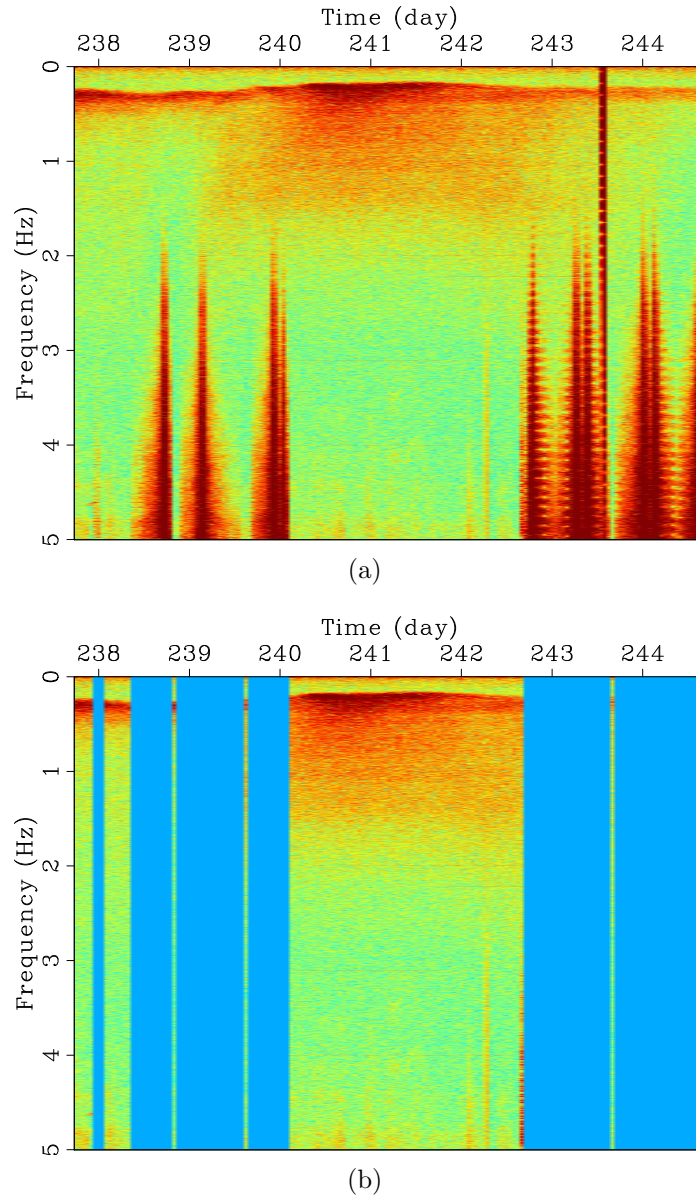
Figure 2: Log-spectrograms for the vertical-component geophone indicated by the western red point in Figure 1. (a) Spectrogram for the entire overlapping period of continuous recordings. Active seismic shooting is distinguished by high amplitudes and comb patterns above 2 Hz. (b) Spectrogram with times of active seismic shooting removed. Warmer colors correspond to higher spectral power. All results in this report use only times without active seismic shooting. [**CR**]

By cross-correlating the recording from one node with recordings from all other nodes, we can create a virtual source gather at any node in the array. For this study, we focus on correlations from the hydrophones and vertical and radial components of the geophones. Because of the effects of attenuation, we only investigate frequencies below 2 Hz, which is reasonable for such a wide-aperture array.

WAVES MODES IN VIRTUAL SOURCE GATHERS

Virtual source gathers derived from passive seismic data reveal three different wave modes: Scholte waves, guided acoustic waves, and critical refractions. We outline evidence for each of these classifications in the following subsections.

Scholte waves

Scholte waves are interface waves that travel along fluid-solid interfaces. Figure 3 shows virtual source gathers for frequencies between $0.2 - 0.4$ Hz for two virtual source locations: one at the western edge of the regular array and one at the eastern edge of the regular array (red dots in Figure 1). The slow event propagating in each gather at a group velocity of approximately 450 m/s (most apparent in the left column of Figure 3) appears to be a Scholte wave for a number of reasons.

First, this event is much stronger in the vertical-vertical (ZZ) correlations (left column; Figure 3) than in the hydrophone-hydrophone (PP) correlations (right column; Figure 3). Since geophones are coupled to the ground while hydrophones are coupled to the water, we expect any Scholte wave propagating along the seabed to be stronger in ZZ correlations than in PP correlations. The stronger, faster-propagating event in the PP correlations is likely an acoustic guided wave (addressed in the following subsection). Second, interface waves typically dominate Earth's ambient seismic noise field at these very low frequencies (microseism band), and as a result Scholte waves are commonly the dominant arrival in passive seismic data collected at the ocean bottom (e.g., Mordret et al., 2013; de Ridder and Biondi, 2015). Third, Scholte waves are commonly observed to propagate at velocities on the order of 100 m/s (e.g., de Ridder and Dellinger, 2011; de Ridder et al., 2015), which is on the order of the group velocities seen here.

Another common characteristic of Scholte waves is that they are dispersive. We create a dispersion image by performing slant stacks for different intercept times and moveout velocities on a virtual source gather, and then performing a Fourier transform along the time axis to produce an image in the frequency-velocity domain. The dispersion image associated with the ZZ virtual source gather in Figure 3a is shown in Figure 4. The phase velocity appears to decrease as frequency increases, which is a typical characteristic of Scholte waves (shorter wavelengths sample slower, shallower depths). Given this dispersion image, it appears that the wavelengths vary
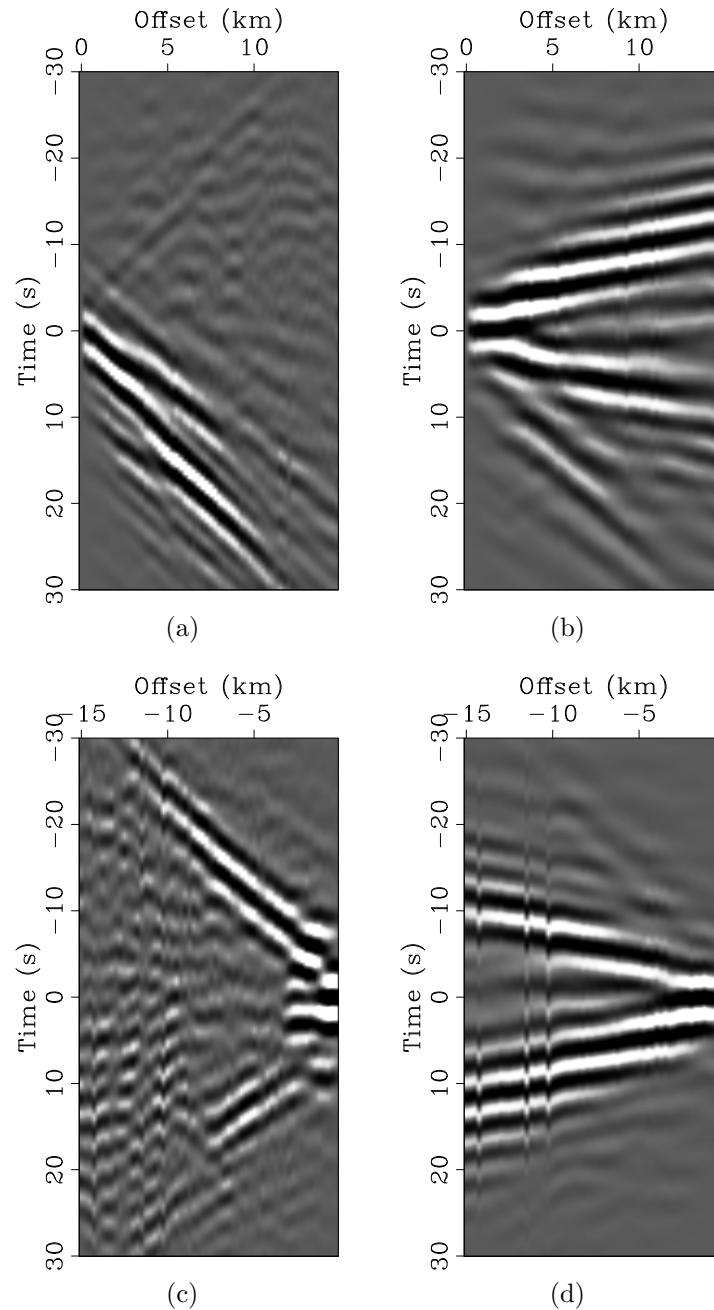
Figure 3: Virtual source gathers for frequencies between $0.2 - 0.4$ Hz. Positive offsets are toward the east while negative offsets are toward the west. Top row: virtual source at the western red dot in Figure 1. Bottom row: virtual source at the eastern red dot in Figure 1. Left column: vertical-vertical geophone correlations. Right column: hydrophone-hydrophone correlations. The strong events in the vertical-vertical geophone correlations are Scholte waves, and their asymmetry suggests they are primarily propagating west to east. Though the same Scholte waves are apparent in the hydrophone-hydrophone correlations, they are faint compared to the faster-propagating acoustic guided waves. [**CR**]

approximately between 1250 m at 0.4 Hz and 3000 m at 0.2 Hz, which are long enough to potentially reach the top of basalt approximately 1 km below the sea bottom.
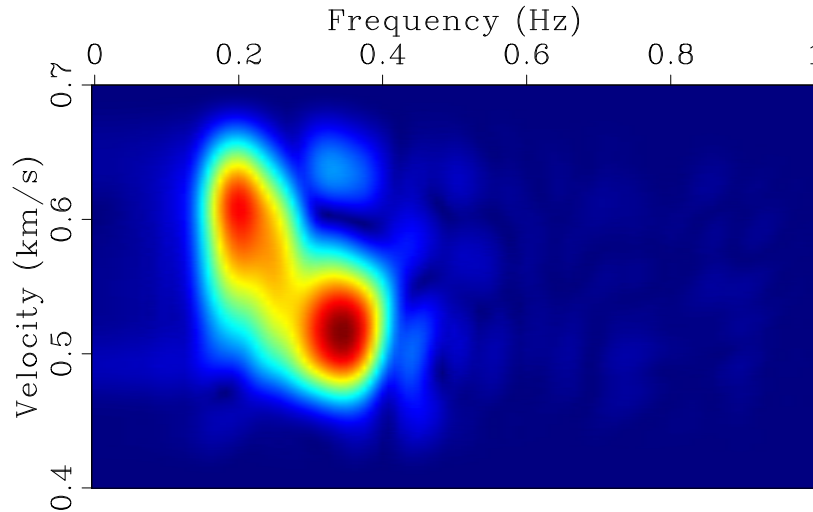

Figure 4: Dispersion image for the virtual source gather centered at the western node for the vertical-vertical components (Figure 3a). Warmer colors correspond to greater coherence of the dispersion estimate. [**CR**]

The previously outlined evidence suggests that these low-velocity, low-frequency events are Scholte waves. From the ZZ correlations (left column; Figure 3), it is clear that the probable Scholte-wave energy is strongest at positive time lags when the virtual source is in the west of the array and at negative time lags when the virtual source is in the east of the array. This indicates that the Scholte-wave energy is propagating primarily from west to east. These Scholte waves can potentially be used to estimate shear-wave velocity depth profiles.

Guided acoustic waves

Guided acoustic waves consist of constructively-interfering, post-critical P-wave reflections trapped between the sea surface and seabed (Burg et al., 1951). They are commonly observed over a broad range of frequencies in active seismic marine surveys where the water depth is shallow and the sea bottom is hard (e.g., Shtivelman, 2004; Klein et al., 2005; Boiero et al., 2013).

Figure 5 shows virtual source gathers for frequencies between $0.4 - 1.5$ Hz for the same two virtual source locations as in Figure 3. The strong, consistent arrivals in each of the panels are likely guided acoustic waves for a number of reasons. First, the group velocity of these arrivals is approximately 1500 m/s, which is the velocity of acoustic waves in water. Given the frequency range here, the velocity is much too high to be associated with Scholte waves. Furthermore, the velocity of these events appears to be the same as the dominant events in the PP correlations at frequencies below 0.4 Hz (right column; Figure 3). Second, the signal-to-noise ratio for this

event appears to be higher in the PP correlations (right column; Figure 5) than in the ZZ correlations (left column; Figure 5), and this same event dominates the PP correlations at frequencies below 0.4 Hz (right column; Figure 3). Since hydrophones are coupled to the water and geophones are coupled to the ground, we expect any waves propagating in the water to be stronger in the PP correlations than in the ZZ correlations.

In terms of kinematics, acoustic guided waves are dispersive and their phase velocities exceed water velocity (Shtivelman, 2004). The background image in Figure 6 shows that the dispersion image derived from the PP virtual source gather in Figure 5b shares these traits. The event is clearly dispersive, as phase velocity for a given mode exceeds water velocity as frequency decreases and approaches water velocity as frequency increases. Additionally, this event displays multiple modes, which has been observed in acoustic guided waves in a number of studies (e.g., Klein et al., 2005; Boiero et al., 2013; Wang et al., 2016).

To further support the hypothesis that these events are acoustic guided waves, We compare the observed dispersion image to theoretical dispersion curves calculated using the following approximation from Hatchell and Mehta (2010) for guided waves in a liquid layer over a solid:

$$\tan\left[\frac{2\pi h f}{c}\sqrt{\frac{c^2}{v_1^2}-1}\right] = -\frac{\rho_2}{\rho_1}\frac{\sqrt{\frac{c^2}{v_1^2}-1}}{\sqrt{1-\frac{c^2}{v_2^2}}}, \tag{2}$$

where h is water depth, ρ_1 and ρ_2 are the densities of water and seafloor, respectively, f is frequency, v_1 is water velocity, v_2 is P-wave velocity of the seafloor, and c is guided-wave phase velocity. Solutions for phase velocity c and frequency f given $h = 1800$ m, $\rho_1 = 1000$ kg/m^3, $\rho_2 = 1800$ kg/m^3, $v_1 = 1500$ m/s, and $v_2 = 2300$ m/s (reasonable parameters given Alves (2017)) are shown in white in Figure 6. The theoretical and observed dispersion curves match quite well, further suggesting that these events are guided acoustic waves.

While commonly observed in shallow marine seismic surveys, guided acoustic waves have rarely been observed in passive seismic data at these frequencies, this spatial scale, and these water depths. One such case was Hatchell and Mehta (2010), who used passive seismic interferometry to recover guided acoustic waves from continuous seismic data recorded by OBNs 1000 m deep and with maximum offset of 9600 m. As seen with the theoretical dispersion curve calculation, though these acoustic guided waves propagate in the water, they interact with the seabed and are thus sensitive to elastic properties of the subsurface material (Klein et al., 2005). It is possible to go beyond the simple half-space P-wave velocity model estimated here by inverting these acoustic guided wave dispersion curves for P-wave velocity depth profiles of the subsurface (Klein et al., 2005; Boiero et al., 2013).
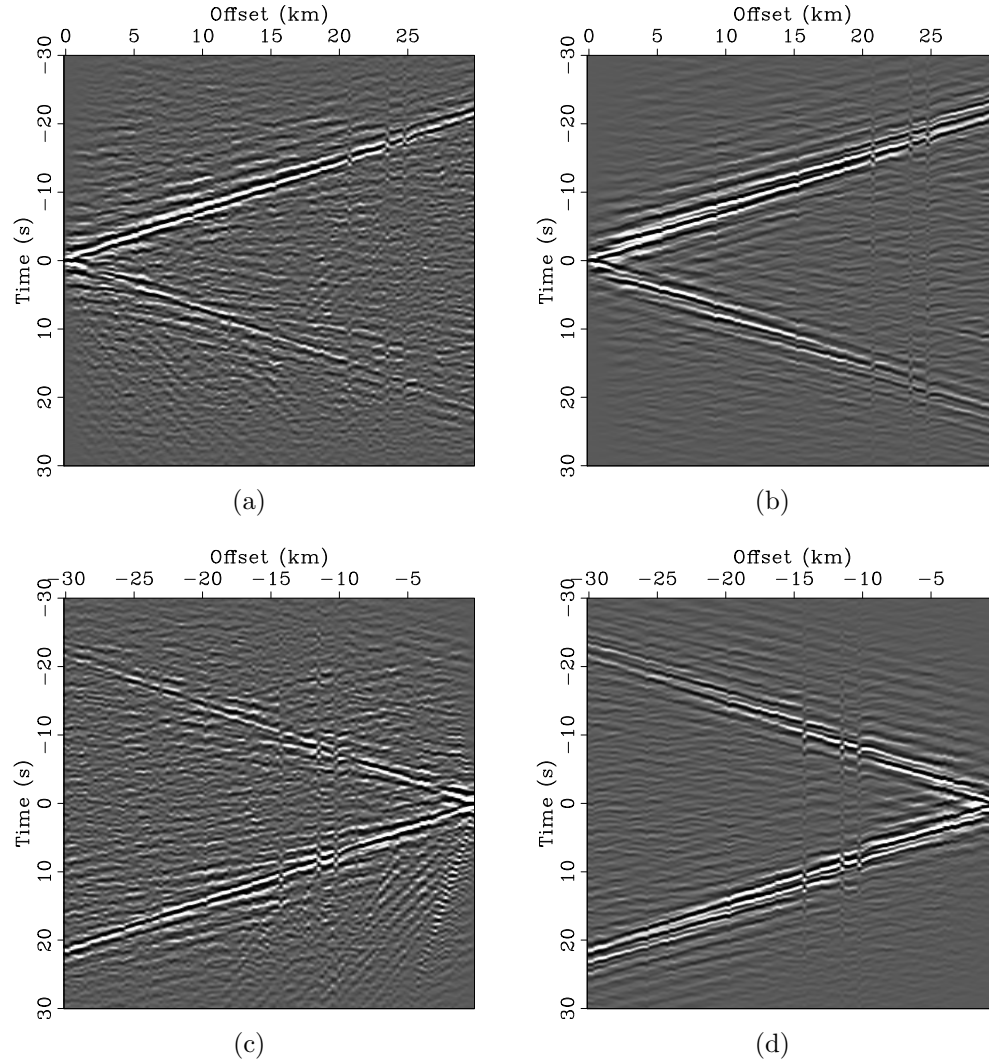
Figure 5: Virtual source gathers for frequencies between $0.4 - 1.5$ Hz. Positive offsets are toward the east while negative offsets are toward the west. Top row: virtual source at the western red dot in Figure 1. Bottom row: virtual source at the eastern red dot in Figure 1. Left column: vertical-vertical geophone correlations. Right column: hydrophone-hydrophone correlations. The strong events in all virtual source gathers are guided acoustic waves propagating at approximately 1500 m/s. Note that the signal-to-noise ratio is much higher in the hydrophone-hydrophone correlations. [**CR**]
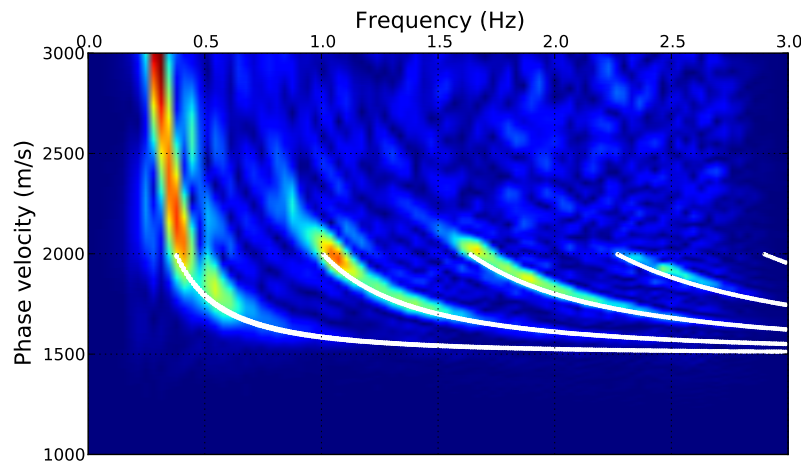
Figure 6: Dispersion image for the virtual source gather centered at the western node for the hydrophone-hydrophone correlations (Figure 5b). A gain proportional to frequency is applied to enhance the higher modes. Warmer colors correspond to greater coherence of the dispersion estimate. The overlying white lines indicate theoretical dispersion curves using Equation 2 and the parameters outlined in the text. Note the similarity between the observed and theoretical dispersion curves. [**CR**]

Critical refractions

Critical refractions occur where there are interfaces with sharp impedance contrasts. At Moere Vest, Alves (2017) identified refractions off the top of basalt using the active data. Here, we examine the passive data for similar critical refractions. The top row of Figure 7 shows time-symmetrized ZZ virtual source gathers for frequencies between $0.5 - 2.0$ Hz for the same two virtual source locations as in Figures 3 and 5. Though faint, there appear to be very fast linear events in both gathers (the stronger events are the acoustic guided waves). The same events in the PP virtual source gathers (not shown here) are even fainter. Because vertical geophones are coupled to the ground and not water, this event is likely propagating in the subsurface. This observation, along with the apparent velocity of the event and knowledge of the subsurface basalt, hints that this event is potentially a critical refraction.

The simplest way to determine whether these events from passive seismic data are critical refractions is to compare them to active-source data. Before doing so, differences in source location must be accounted for: virtual sources are located at nodes on the sea bottom, while active sources are located near the sea surface. To get two gathers to correspond to the same location, we reference the virtual source gather from passive data and the receiver gather from active data to a common node. To get the gathers to start at the same time, we shift the receiver gather from active data by 1 s. Given that water depth at Moere Vest is approximately $1600 - 1900$ m, this shift removes the initial traveltime from sea-surface source to sea-bottom node

and effectively places the active sources near the sea bottom. Though the angle of incidence of the initial path through the water column depends on source-receiver offset, we assume that it does not vary significantly from normal incidence due to ray bending from the high impedance contrast between the seabed and water.

Active-source vertical-geophone receiver gathers centered at the western and eastern nodes of the regular spread are shown in the bottom row of Figure 7. We bandpass for frequencies between $2-6$ Hz, apply a linear gain proportional to offset, and heavily clip the gathers to enhance the critical refractions. Comparison of these events to the fast linear events in the corresponding ZZ virtual source gathers in the top row of Figure 7 reveals similar arrival times and moveout velocities. The similarity not only includes the first linear arrivals, but also the later linear arrivals, which may be multiple-related critical refractions.

To enhance the stacking power of the potential critical refraction events in the passive data, it is common to stack over all virtual source gathers to create a super-source gather (Lin et al., 2013; Nakata et al., 2015). The trade-off is that all spatial information is lost, as the process effectively assumes a 1D medium. The ZZ super-source gather (Figure 8a) reveals stronger critical refractions than in the individual virtual source gathers (top row; Figure 7). These events are apparent at both negative and positive times, as well as both positive and negative offsets, which indicates that the potential refractions are propagating in both directions along the array. The symmetry of these events in time and space suggest that they are not generated by localized sources, and that their fast velocities are not just apparent velocities from waves hitting the array broadside. The vertical-radial (ZR) super-source gather (Figure 8b) also displays hints of a refraction-like event that was not apparent in corresponding individual virtual source gathers (not shown in this report). Compared to the ZZ super-source gather, the fast linear events arrive later in time and are only apparent at positive time lags. The latter observation could provide insight into how these potential critical refractions are generated in Earth's ambient seismic noise field, as they suggest that refractions only appear when passing the vertical geophone before the radial geophone (and not vice versa).

To further examine the difference in arrival times of the potential refraction in the super-source gathers, we compare their positive time lags to vertical- and radial-component receiver gathers from active data (Figure 9). Though the super-source gathers do not correspond to a specific spatial location and these particular receiver gathers are centered at the western node of the regular array, it is an adequate comparison for investigating the relative arrival times of the critical refraction between different geophone components. The arrival times of the potential refraction event in the ZZ super-source gather and vertical-component receiver gather are similar (left column; Figure 9). Using these arrival times as a reference, it is clear that the fast linear events arrive later in the ZR super-source gather and the radial-component receiver gather by similar amounts of time (right column; Figure 9). Moronfoyer et al. (2016) hypothesized that the difference in arrival times of the refraction in the two orthogonal components was due to differences in subsurface P-wave and S-wave
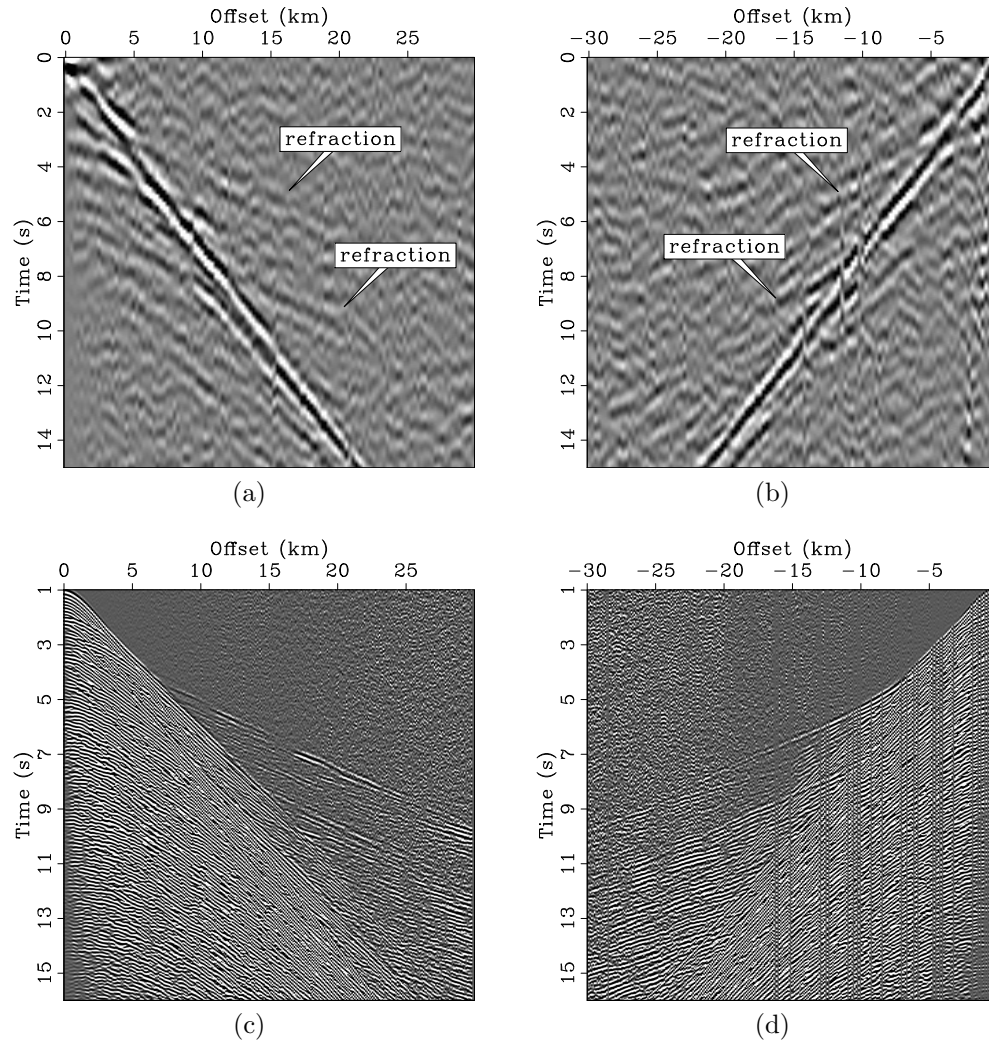
Figure 7: Comparison of virtual source gathers from passive data and receiver gathers from active-source data . Left column: western node in Figure 1. Right column: eastern node in Figure 1. Top row: virtual source gathers between vertical-vertical components for frequencies between $0.5 - 2.0$ Hz. Gathers are symmetrized over zero-time lag to enhance fast linear events. Bottom row: vertical-component receiver gathers from active data for frequencies between $2 - 6$ Hz. A strong clip and a gain proportional to offset are applied to enhance refractions, and the gathers are shifted in time by 1 s so they are comparable to the virtual source gathers. The arrival times of the refraction events in the passive and active gathers coincide well. [**CR**]
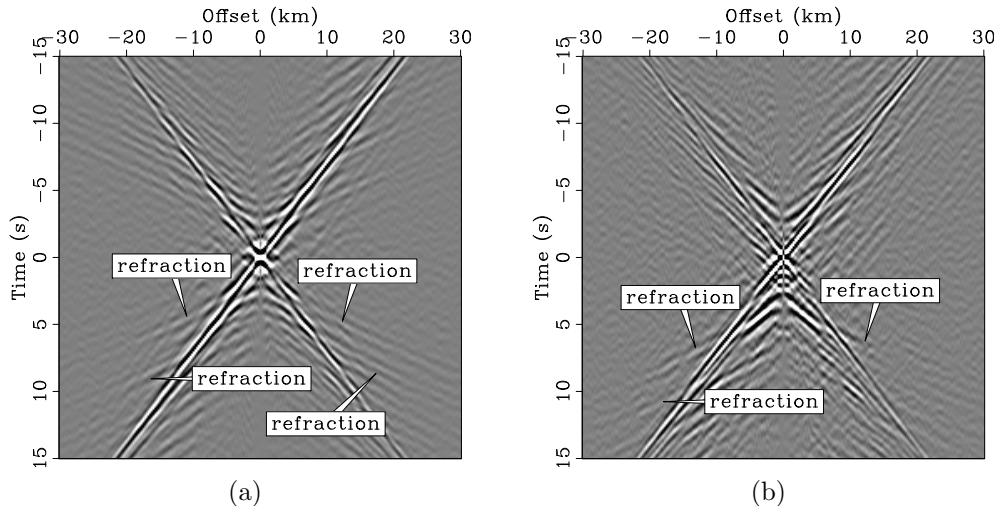
Figure 8: Virtual super-source gathers for frequencies between $0.5 - 2.0$ Hz. (a) Vertical-vertical geophone correlations. (b) Vertical-radial geophone correlations. Note the difference in the first refraction arrival times between the two gathers, particularly at positive time lags. [**CR**]

velocities. The vertical component recorded the faster P-wave refraction while the radial component recorded the slower converted S-wave refraction. Regardless of the true reason for the differences in refraction arrival times, the fact that fast linear events in the ZZ and ZR super-source gathers display similar arrival time differences as in the active data is another piece of evidence supporting the classification of these events as critical refractions.

To compare the velocities of the apparent refractions in the passive and active data, we perform linear moveout on the gathers in Figure 9. Results using a moveout velocity of 4400 m/s are shown in Figure 10. The apparent refraction in the super-source gathers and receiver gathers (at least at positive offsets) appear to be flattened, thus providing another piece of evidence that we are recovering critical refractions in the passive data. Note that the refractions in the receiver gathers are not quite flat at negative offsets (where sources are west of the node); they require moveout with a higher velocity to be flattened. This could be because the basalt tilts slightly downward toward the west, and apparent refraction velocities are typically slower shooting down-dip (toward the west) than up-dip (toward the east).

This trend is not observed in the super-source gathers. This is potentially because the negative offsets in the super-source gathers are sensitive to a different part of the basalt than the negative offsets of the receiver gather centered at the western node of the regular array. Because of the relatively large number of nodes in the regular section of the array, both offsets of the super-source gathers are biased towards the refraction response off the basalt directly beneath that particular subset of the array. While the positive offsets of the receiver gather centered at the western node of the regular array sense the same refraction off the basalt beneath the regular array, the
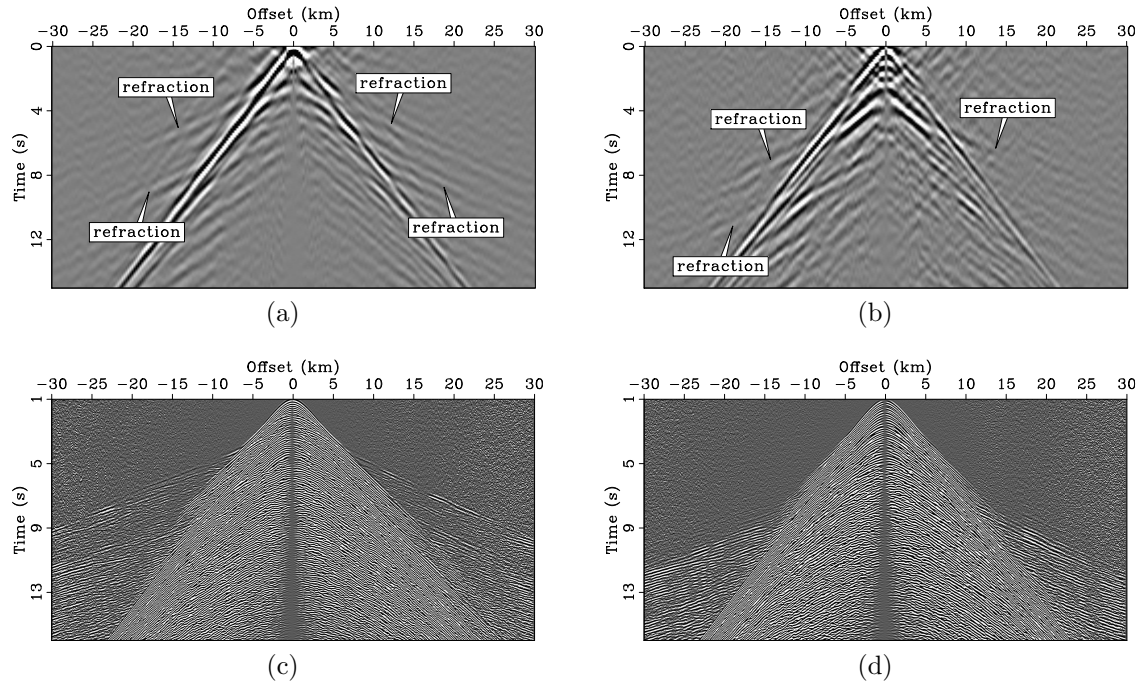
Figure 9: Comparison of virtual super-source gathers from passive data to receiver gathers from active-source data. Positive time lags of virtual super-source gather for frequencies between $0.5 - 2.0$ Hz: (a) vertical-vertical components, and (b) vertical-radial components. Receiver gathers from active-source data centered at the western node in Figure 1 for frequencies between $2 - 6$ Hz: (c) vertical component, and (d) radial component. A strong clip and a gain proportional to offset are applied to enhance refractions, and the gathers are shifted in time by 1 s so they are comparable to the virtual source gathers. Note the later refraction arrival times when looking at gathers involving the radial component. [**CR**]

negative offsets sense the refraction off the basalt that is west of the regular array. As a result, the negative offsets of the receiver gather are not flattened at 4400 m/s while the positive offsets and super-source gathers are.
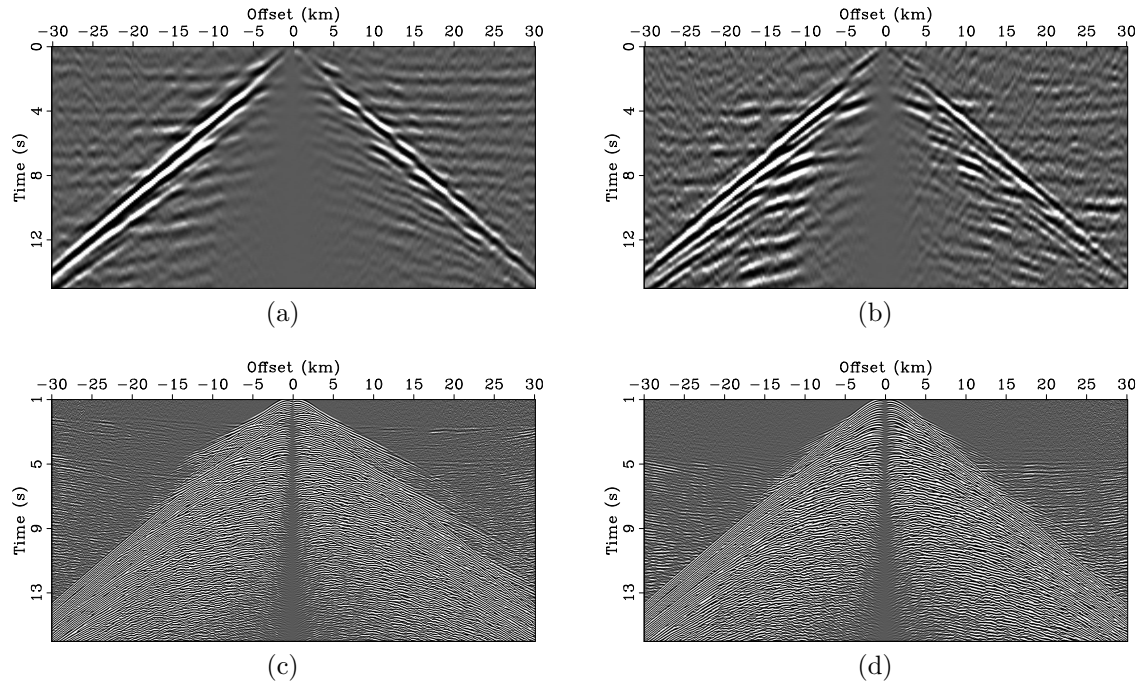

Figure 10: Linear move-out of the gathers in Figure 9 with a velocity of 4400 m/s. Note how the refraction events in all gathers are flattened. [**CR**]

Overall, there is evidence that we are extracting critical refractions from passive data, particularly when comparing these events to active data. To the author's knowledge, these types of events from passive data have never been observed before. They are observed at Moere Vest for a couple of potential reasons. One is that the array provides sufficiently long offsets for potential refractions to become well-separated from other events, such as guided acoustic waves here. Another reason is that there is a basalt body in the subsurface, which is likely to produce the high-impedance interface needed for critical refractions to be generated. We investigate one hypothesis for the generation of critical refractions in passive energy in the next section.

MODELING OF CRITICAL REFRACTIONS

While we appear to observe critical refractions at Moere Vest, the mechanism for their generation is not yet understood. Knowing that Earth's ambient seismic field is dominated by interface waves, one hypothesis is that we are observing Scholte waves that are interacting with the top of basalt and subsequently converting or scattering into critical refractions and diffractions. Given it appears that the Scholte-wave wavelengths vary approximately between 1250 m at 0.4 Hz and 3000 m at 0.2 Hz, it is possible that they penetrate deep enough to sense the basalt's horst-and-graben

structure approximately 1 km beneath the sea bottom. To test this hypothesis, we simulate wavefield conversions using a staggered-grid elastic finite-difference wave propagation code (Fabien-Ouellet et al., 2017) on a simplified 2D elastic model of Moere Vest consisting of three layers: a water layer, an overburden layer, and a basalt layer with a 100-m thick step feature (Figure 11). Specific values for the elastic parameters were estimated from Alves (2017) and can be found in Table 1. The model spans 1500 cells in the horizontal direction and 400 cells in the vertical direction, and has a grid spacing of 100 m. Because we are interested in observing the interaction of low-frequency Scholte waves with the simple step feature of the top of basalt, we place an explosive source with 0.4 Hz central frequency 50 km away from the step feature and 100 m below the sea bottom so that the Scholte wave is separated from other wave modes (refractions and direct waves) by the time it reaches the step feature. We also place absorbing boundary conditions along all sides of the model, as we want to reduce interference from waves reflecting off the sea surface. We run the propagation for 12500 time steps of size 0.008 s.

Layer	Thickness [m]	V_p [m/s]	V_s [m/s]	Density [kg/m^3]
Water	1500	1500	0	1000
Overburden	1000	2300	1400	1800
Basalt	infinite	5000	3000	2500

Table 1: Model parameters for the simple three-layer model with a 100-m thick step feature at the top of basalt shown in Figure 11.

Figure 12a shows the resulting vertical-velocity source gather recorded by receivers along the water bottom. While there are a number of arrivals in the gather, many of them can be grouped together by apparent moveout velocity and are likely to be related to trying to excite a very low-frequency source in a relatively thin layer. To help identify these events, we include a snapshot of the vertical-velocity wavefield at 24 s in Figure 13. The fastest group of arrivals are likely related to the critical refraction off the top of basalt as they are traveling at approximately 5000 m/s (150000 m/30 s), which is the P-wave velocity of the basalt layer. The slower bound of this group of arrivals is likely the direct P-wave as it is propagating at approximately 2500 m/s (150000 m/60 s), which is close to the P-wave velocity of the overburden. Additionally, the corresponding event at 60 km in Figure 13 extends through the entirety of the basalt, further suggesting that this is a direct P-wave. The slower group of arrivals is likely related to Scholte waves. Though their moveout velocities appear to be approximately 1400 m/s (140000 m/100 s), which is the S-wave velocity in the overburden, the corresponding wavefield trapped near the surface around 24 km in Figure 13 suggests that these arrivals are related to interface waves.

Assuming the slower packet of arrivals is related to Scholte waves, there is apparent forward- and back-scattered energy at the location of the step feature (50 km). To better examine the scattered events, we subtract the source gather associated with the basalt with the step feature (Figure 12a) from a source gather associated with the basalt without the step feature (not shown here). While there is similar forward-
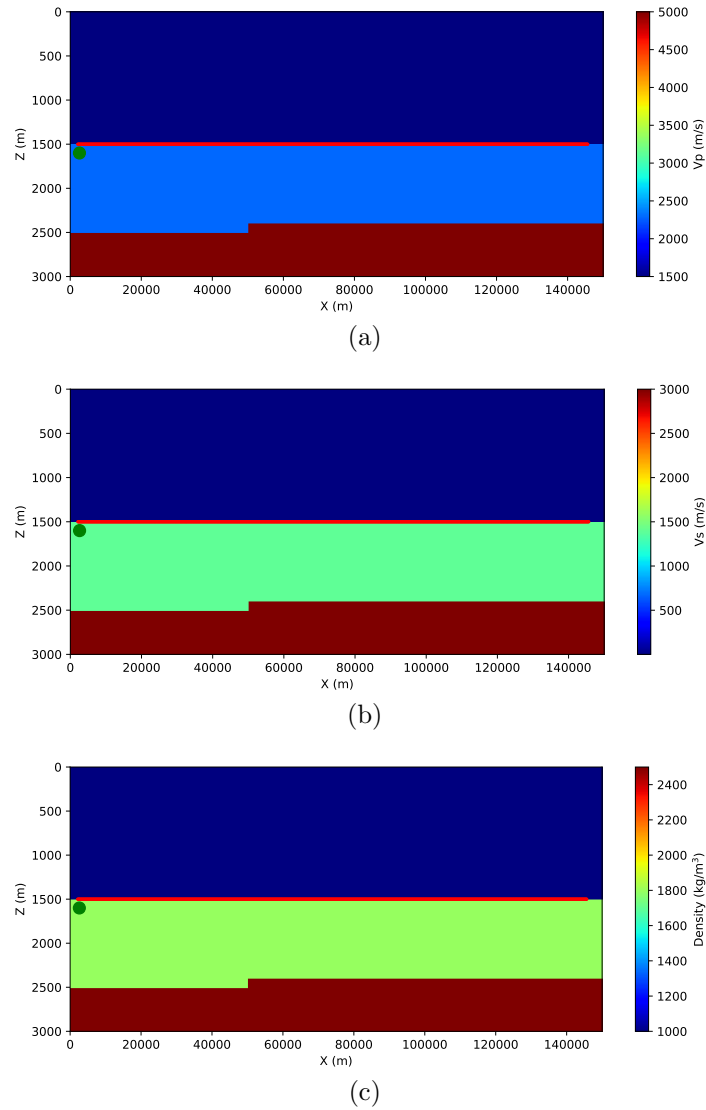
Figure 11: Model used for generating synthetic source gathers. The simple three-layer model consists of a water layer, an overburden, and a basalt body with a step feature. (a) P-wave velocity. (b) S-wave velocity. (c) Density. Red dots represent receiver locations, while green dots represent source locations. Note that vertical and horizontal axes are not to scale in order to enhance the step feature in the basalt. [**CR**]

and back-scattering energy associated with the faster refraction packet and the slower Scholte-wave packet (Figure 12b), we focus on the scattered events associated with the Scholte wave. As expected, there is back-scattered energy with a similar moveout velocity as the incident Scholte wave; this is likely a back-scattered Scholte wave. More importantly, there is both forward- and back-scattered energy with similar moveout velocity as the earlier-arriving incident critical refractions. This seems to suggest that a Scholte wave interacting with a step feature as thin as 100 m can produce forward- and back-scattered critical refractions. Thus, it is possible that a low-frequency Scholte wave interacting with the horst-and-graben structure of the top of basalt could produce critical refractions along both directions of the array.
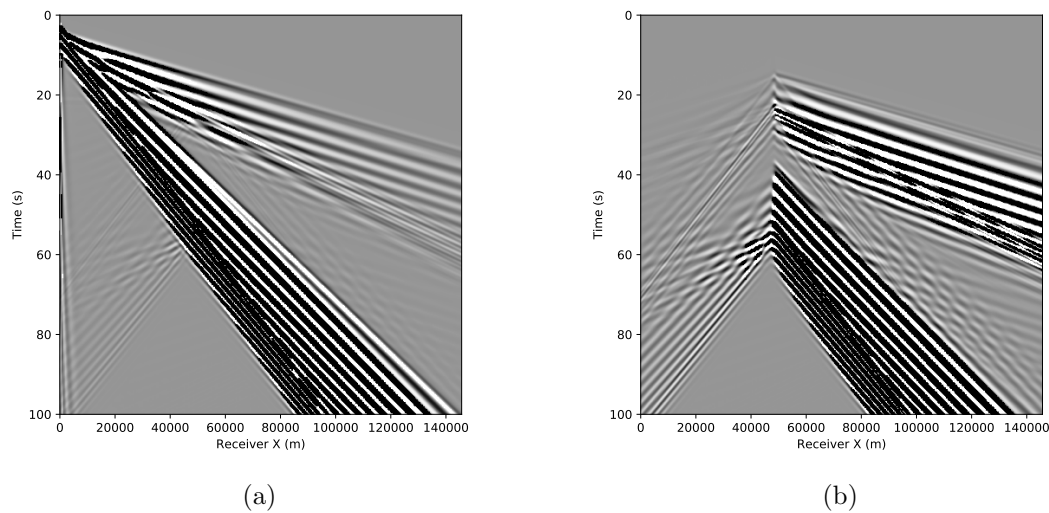

(a)　　　　　　　　　　　　　　　　(b)

Figure 12: (a) Vertical-velocity source gather associated with the model in Figure 11. (b) Difference between vertical-velocity source gathers with and without the step feature at the top of basalt. Note the back-scattered energy from the step feature appears to be comprised of both interface waves and refractions. The source wavelet is a Ricker wavelet with 0.4 Hz central frequency. [**CR**]

CONCLUSIONS

Using seismic interferometry, we found that the continuous seismic recordings from the Moere Vest OBN array contained apparent Scholte waves, guided acoustic waves, and critical refractions. While Scholte waves are commonly extracted from Earth's ambient seismic noise field, the latter two wave modes are not. Acoustic guided waves are commonly observed in shallow-water active seismic surveys, but had rarely been observed in passive data at low frequencies and deep depths. At Moere Vest, we found that the dispersion image for the passive acoustic guided wave had similar characteristics as those from typical active seismic surveys. Much like Scholte waves, these dispersion curves can be inverted for depth profiles of seismic velocities. Even
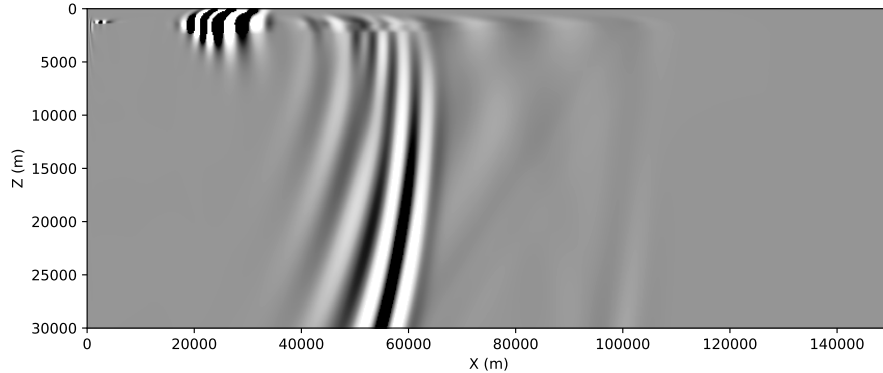
Figure 13: Snapshot of the vertical-velocity wavefield through the model in Figure 11 at 24 s. Note the apparent refraction at 100 km, the apparent direct P-wave at 60 km, and the apparent Scholte wave at 24 km. Though the top of basalt is at 2.5-km depth, the displayed depth goes down to 30 km to more easily observe the characteristics of the wavefield. Note that the horizontal and vertical axes are not to scale. [**CR**]

more rare are critical refractions, which had never been observed in passive seismic data before. We found that the arrival times of potential critical refractions from passive data compared well to those from active data. It is likely that the length of the array, the presence of a high-impedance interface at the top of basalt, and the horst-and-graben structure of the top of basalt allows these events to be visible.

Future work will focus on understanding the mechanism of these critical refractions and using them for subsurface imaging. Of primary interest is further understanding how Earth's ambient seismic field could generate these events. While the forward modeling of the wavefield here supports the primary hypothesis that we are observing deep-penetrating Scholte waves that converted into critical refractions off the horst-and-graben structured top of basalt, there are other possible hypotheses to test. One such hypothesis is that these critical refractions are due to the interaction of acoustic guided waves with the top of basalt. In addition to further modeling the critical refractions, we also intend to use these wave modes to estimate subsurface properties. For the Scholte and acoustic guided waves, the associated dispersion curves could be inverted to obtain depth profiles of $V_p - V_s$ ratios. For the critical refractions, we will need to investigate processing techniques (such as phase-weighted stacking or creating a selection filter as in Nakata et al. (2015)) to enhance these arrivals in individual virtual source gathers in hopes they may then be used for body-wave imaging.

ACKNOWLEDGEMENTS

REFERENCES

Alves, G., 2017, Elastic Full Waveform Inversion of the Moere Vest data: SEP-Report, **168**, 63–76.

Bensen, G., M. Ritzwoller, M. Barmin, A. Levshin, F. Lin, M. Moschetti, N. Shapiro, and Y. Yang, 2007, Processing seismic ambient noise data to obtain reliable broadband surface wave dispersion measurements: Geophysical Journal International, **169**, 1239–1260.

Bensen, G., M. Ritzwoller, and N. Shapiro, 2008, Broadband ambient noise surface wave tomography across the United States: Journal of Geophysical Research: Solid Earth, **113**.

Boiero, D., E. Wiarda, and P. Vermeer, 2013, Surface-and guided-wave inversion for near-surface modeling in land and shallow marine seismic data: The Leading Edge.

Brooks, L. A. and P. Gerstoft, 2009, Green's function approximation from cross-correlations of 20–100 Hz noise during a tropical storm: The Journal of the Acoustical Society of America, **125**, 723–734.

Burg, K., M. Ewing, F. Press, and E. Stulken, 1951, A seismic wave guide phenomenon: Geophysics, **16**, 594–612.

Chang, J. P., 2017, The search for P-waves at Forties: SEP-Report, **168**, 35–50.

Chang, J. P., S. A. de Ridder, and B. L. Biondi, 2016, High-frequency Rayleigh-wave tomography using traffic noise from Long Beach, California: Geophysics, **81**, B1–B11.

de Ridder, S., 2014, Analysis of moere vest obns as continuous data: SEP-Report, **155**, 71–80.

de Ridder, S., B. Biondi, and D. Nichols, 2015, Elliptical-anisotropic eikonal phase velocity tomography: Geophysical Research Letters, **42**, 758–764.

de Ridder, S. and J. Dellinger, 2011, Ambient seismic noise eikonal tomography for near-surface imaging at Valhall: The Leading Edge, **30**, 506–512.

de Ridder, S. A. and B. L. Biondi, 2015, Ambient seismic noise tomography at ekofisk: Geophysics.

Draganov, D., X. Campman, J. Thorbecke, A. Verdel, and K. Wapenaar, 2013, Seismic exploration-scale velocities and structure from ambient seismic noise (¿ 1 Hz): Journal of Geophysical Research: Solid Earth, **118**, 4345–4360.

Fabien-Ouellet, G., E. Gloaguen, and B. Giroux, 2017, Time-domain seismic modeling in viscoelastic media for full waveform inversion on heterogeneous computing platforms with OpenCL: Computers & Geosciences, **100**, 142–155.

Gerstoft, P., P. M. Shearer, N. Harmon, and J. Zhang, 2008, Global P, PP, and PKP wave microseisms observed from distant storms: Geophysical Research Letters, **35**.

Hatchell, P. and K. Mehta, 2010, Ocean bottom seismic (obs) timing drift correction using passive seismic data, *in* SEG Technical Program Expanded Abstracts 2010, 2054–2058, Society of Exploration Geophysicists.

Klein, G., T. Bohlen, F. Theilen, S. Kugler, and T. Forbriger, 2005, Acquisition and inversion of dispersive seismic waves in shallow marine environments: Marine Geophysical Researches, **26**, 287–315.

Lin, F.-C., D. Li, R. W. Clayton, and D. Hollis, 2013, High-resolution 3D shallow crustal structure in Long Beach, California: Application of ambient noise tomography on a dense seismic array: Geophysics, **78**, Q45–Q56.

Mordret, A., M. Landès, N. Shapiro, S. Singh, P. Roux, and O. Barkved, 2013, Near-surface study at the valhall oil field from ambient noise surface wave tomography: Geophysical Journal International, ggt061.

Moronfoyer, A. T., S. Ronen, S. L. Klemperer, and G. Alves, 2016, Upper-crustal structure of the Møre margin, offshore-norway: 20016 AGU Fall Meeting, San Francisco, –.

Nakata, N., J. P. Chang, J. F. Lawrence, and P. Boué, 2015, Body wave extraction and tomography at long beach, california, with ambient-noise interferometry: Journal of Geophysical Research: Solid Earth, **120**, 1159–1173.

Nakata, N., R. Snieder, T. Tsuji, K. Larner, and T. Matsuoka, 2011, Shear wave imaging from traffic noise using seismic interferometry by cross-coherence: Geophysics, **76**, SA97–SA106.

Poli, P., M. Campillo, H. Pedersen, et al., 2012, Body-wave imaging of Earths mantle discontinuities from ambient seismic noise: Science, **338**, 1063–1065.

Roux, P., K. G. Sabra, P. Gerstoft, W. Kuperman, and M. C. Fehler, 2005, P-waves from cross-correlation of seismic noise: Geophysical Research Letters, **32**.

Ruigrok, E., X. Campman, and K. Wapenaar, 2011, Extraction of P-wave reflections from microseisms: Comptes Rendus Geoscience, **343**, 512–525.

Seats, K. J., J. F. Lawrence, and G. A. Prieto, 2012, Improved ambient noise correlation functions using Welch's method: Geophysical Journal International, **188**, 513–523.

Shapiro, N. M., M. Campillo, L. Stehly, and M. H. Ritzwoller, 2005, High-resolution surface-wave tomography from ambient seismic noise: Science, **307**, 1615–1618.

Shtivelman, V., 2004, Estimating seismic velocities below the sea-bed using surface waves: Near Surface Geophysics, **2**, 241–247.

Wang, J., R. R. Stewart, N. I. Dyaur, and M. L. Bell, 2016, Marine guided waves: Subbottom property estimation and filtering using physical modeling data: Geophysics.

Wapenaar, K., D. Draganov, R. Snieder, X. Campman, and A. Verdel, 2010, Tutorial on seismic interferometry: Part 1–basic principles and applications: Geophysics, **75**, 75A195–75A209.

Zhan, Z., S. Ni, D. V. Helmberger, and R. W. Clayton, 2010, Retrieval of Moho-reflected shear wave arrivals from ambient seismic noise: Geophysical Journal International, **182**, 408–420.